

Molecular model of the ferroportin intracellular gate and implications for the human iron transport cycle and hemochromatosis type 4A

Julie Guellec,^{*,†} Ahmad Elbahnsi,[‡] Marlène Le Tertre,^{*,§} Kévin Uguen,^{*,§} Isabelle Gourlaouen,^{*} Claude Férec,^{*,†,§} Chandran Ka,^{*,§,¶} Isabelle Callebaut,^{‡,1} and Gérald Le Gac^{*,§,¶,1,2}

^{*}INSERM Unité Mixte de Recherche (UMR) 1078, Etablissement Français du Sang–Bretagne, Institut Brestois Santé-Agro-Matière, Université Bretagne Loire–Université de Brest, Brest, France; [†]Association Gaetan Saleun, Brest, France; [‡]Muséum National d’Histoire Naturelle, UMR Centre National de la Recherche Scientifique (CNRS) 7590, Institut de Minéralogie, de Physique des Matériaux et de Cosmochimie, Institut de Minéralogie, de Physique des Matériaux et de Cosmochimie (IMPMC), Sorbonne Université, Paris, France; [§]Service de Génétique Médicale, Centre Hospitalier Régional et Universitaire (CHRU) de Brest, Hôpital Morvan, Brest, France; and [¶]Laboratory of Excellence Laboratory of Excellence (GR-Ex), Paris, France

ABSTRACT: Ferroportin 1 (FPN1) is a major facilitator superfamily transporter that is essential for proper maintenance of human iron homeostasis at the systemic and cellular level. FPN1 dysfunction leads to the progressive accumulation of iron in reticuloendothelial cells, causing hemochromatosis type 4A (or ferroportin disease), an autosomal dominant disorder that displays large phenotypic heterogeneity. Although crystal structures have unveiled the outward- and inward-facing conformations of the bacterial homolog *Bdellovibrio bacteriovorus* Fpn (or Bd2019) and calcium has recently been identified as an essential cofactor, our molecular understanding of the iron transport mechanism remains incomplete. Here, we used a combination of molecular modeling, molecular dynamics simulations, and Ala site-directed mutagenesis, followed by complementary *in vitro* functional analyses, to explore the structural architecture of the human FPN1 intracellular gate. We reveal an interdomain network that involves 5 key amino acids and is likely very important for stability of the iron exporter facing the extracellular milieu. We also identify inter- and intradomain interactions that rely on the 2 Asp84 and Asn174 critical residues and do not exist in the bacterial homolog. These interactions are thought to play an important role in the modulation of conformational changes during the transport cycle. We interpret these results in the context of hemochromatosis type 4A, reinforcing the idea that different categories of loss-of-function mutations exist. Our findings provide an unprecedented view of the human FPN1 outward-facing structure and the particular function of the so-called “gating residues” in the mechanism of iron export.—Guellec, J., Elbahnsi, A., Le Tertre, M., Uguen, K., Gourlaouen, I., Férec, C., Ka, C., Callebaut, I., Le Gac, G. Molecular model of the ferroportin intracellular gate and implications for the human iron transport cycle and hemochromatosis type 4A. *FASEB J.* 33, 000–000 (2019). www.fasebj.org

KEY WORDS: MFS transporters • gating residues • alternating access mechanism • molecular dynamics simulations • iron metabolism

Ferroportin 1 (FPN1, also referred to as SLC40A1; Uniprot Q9NP59) is the only known iron exporter in mammals and is considered to be a key player in both cellular and systemic iron homeostasis (1–3). FPN1 is expressed in all

types of cells that handle major iron flow, including macrophages, duodenal enterocytes, hepatocytes, and placenta syncytiotrophoblasts (4). Cell surface expression is predominantly regulated by the liver-derived peptide hepcidin (5), which induces internalization and degradation of FPN1, decreasing iron delivery to plasma (2). The hepcidin-ferroportin axis plays an important role in the pathogenesis of inherited and acquired iron metabolism disorders, including iron overload diseases and iron-restricted anemia (6).

FPN1 dysfunction is responsible for hemochromatosis type 4, an inborn error of iron metabolism that is transmitted as an autosomal dominant trait, and is characterized by wide clinical heterogeneity. This is only partially explained by the existence of mutations with opposing effects. Patients with loss-of-function mutations usually

ABBREVIATIONS: β -gal, β -galactosidase; 3D, 3-dimensional; BbFpn, *Bdellovibrio bacteriovorus* Fpn; FPN1, ferroportin 1; HEK, human epithelial kidney; MD, molecular dynamic; MFS, major facilitator superfamily; TM, transmembrane; WT, wild type

¹ These authors contributed equally to this work.

² Correspondence: Centre Hospitalier Régional Universitaire de Brest, Hôpital Morvan, Bat 5bis, Laboratoire de Génétique Moléculaire et d’Histocompatibilité, 2 Ave. Foch, 29200 Brest, France. E-mail: gerald.legac@univ-brest.fr

doi: 10.1096/fj.201901857R

This article includes supplemental data. Please visit <http://www.fasebj.org> to obtain this information.

present mesenchymal or mixed iron overload (corresponding to early iron deposition within Kupffer cells) and markedly elevated serum ferritin concentrations contrasting with normal or transferrin saturation levels. This phenotypic presentation is commonly referred to as ferroportin disease, or hemochromatosis type 4A. Gain-of-function mutations, which are less frequent, result in partial to complete resistance to hepcidin; patients usually display elevated transferrin saturation levels. Hyperferritinemia is secondary to plasma iron burden and is mostly associated with iron deposits in hepatocytes. These biologic and histologic features mimic the natural history of HFE-related hemochromatosis; hence, gain-of-function FPN1 mutations are associated with hemochromatosis type 4B.

Important progress has been made these last 5 yr in understanding FPN1 structural biology. We and others first provided evidence of the relatedness of FPN1 to the major facilitator superfamily (MFS) (7–9). The MFS structural core consists of 12 transmembrane (TM) helices organized into 2 structurally similar domains: N-domain (TM1–TM6) and C-domain (TM7–TM12) (10). Taniguchi *et al.* then identified Bd2019 [*Bdellovibrio bacteriovorus* Fpn (BbFpn) (11)] as a bacterial homolog of the human iron exporter and solved its structures in both the outward- and inward-facing states (12). The X-ray structures of BbFpn confirmed the typical MFS fold and provided important clues about the mechanism of iron egress and FPN1 regulation by hepcidin. Deshpande *et al.* (13) very recently reported the crystal structure of Ca²⁺-bound BbFpn in an inward-facing conformation and demonstrated that human FPN1 iron transport activity is dependent on extracellular Ca²⁺. The authors proposed an alternate access mechanism, which is characteristic of MFS transporters (10, 14), to explain how iron is exported by FPN1 across the plasma membrane, comprising 3 fundamental steps: 1) in the outward-facing structure, Ca²⁺ binds to FPN1 and initiates a conformational change that enables transition from open outward-facing to open inward-facing states; 2) in the inward-facing structure, Fe²⁺ binds to FPN1 and triggers a return to the outward-facing open state; and 3) in the extracellular milieu, Fe²⁺ is oxidized to Fe³⁺, which is taken up by the plasma transferrin and delivered to various tissues throughout the body (2).

Fundamental questions still remain unanswered about the molecular mechanisms associated with the conformational changes underlying the iron transport cycle, as well as on those ensuring the stability of the outward- and inward-facing conformations. In MFS transporters, a set of specific, so-called “gating” residues, has been suggested to be the key actor in interactions between helices from the N- and C-domains that alternately move to form the outward- and inward-facing conformations, as well as a series of intermediate states (10). Salt bridges and hydrogen bonds are considered particularly important for stabilizing MFS transporters in the outward-facing state. In line with this idea, we recently provided evidence of the formation of a noncovalent, electrostatic interaction between Arg178 and Asp473 on the intracellular side of human FPN1. After also investigating phenotypes related to the recurrent p.Arg178Gln missense mutation, we postulated that the

shift of the equilibrium toward the inward-facing state because of a deficient role of gating residues in the intracellular gate could represent a new molecular mechanism of loss of FPN1 function (15).

Here, using comparative modeling and molecular dynamic (MD) simulations, we predict atomic details for the organization of human FPN1 in the outward-facing open state. *In vitro* evaluation of Ala mutants in different TM helices is interpreted relative to the expected role of the corresponding nonmutated residues in forming noncovalent bonds (salt bridges or hydrogen bonds) between the N-domain and the C-domain of human FPN1. We identified 5 key residues that play an essential function in the intracellular gate and iron transport cycle. Comparing BbFpn and FPN1 3-dimensional (3D) structures revealed interactions that may play an important role in the stability of the gate and in the modulation of the conformational changes in the human transporter, some of which cannot be formed in the bacterial homolog. We finally highlight some critical residues that are mutated in patients with a typical hemochromatosis type 4A phenotype.

MATERIALS AND METHODS

Modeling and MD simulations

As previously reported (15), a model of the 3D structure of human FPN1 was built using Modeler v.9.15 (16) considering the sequence alignment reported by Taniguchi *et al.* (12) and, as template, the experimental 3D structure of *B. bacteriovorus* iron transporter Bd2019 in an outward-facing conformation (Protein Data Bank 5AYM). Some large regions were discarded from the FPN1 model because no template was available for accurate modeling: aa 1 to 21 (N-terminal sequence), aa 237–301 (linker between the N- and the C-domain), and aa 396–450 (TM9–TM10 loop).

An MD simulation was run for 100 ns using the human FPN1 3D structure model. This was embedded in a membrane bilayer composed of 2-oleoyl-1-palmitoylsn-glycero-3-phosphocholine molecules and solvated within a rectangular box of explicit water molecules and 15 mM NaCl. The simulation box (105 × 105 × 100 Å³) contained the protein, 275 lipids, 49 Na⁺ ions (18), 53 Cl[−] ions (19), and 18,409 TIP3P water molecules regularly filling the pore and the full box. (20) Minimization, equilibration, and production phases or steps used the Chemistry at Harvard Macromolecular Mechanics (CHARMM36) force field (21, 22) in Not Another Molecular Dynamics (NAMD) 2.9 (23) following the protocol described in Hoffmann *et al.* (17). The root mean square deviations between the initial model and each snapshot from the MDs are given in Supplemental Fig. S2. The time of 25 ns appeared sufficient to achieve stable models. Distances between some atoms from critical amino acids along the simulation are provided in Fig. 4.

An additional simulation was carried out with 70 mM CaCl₂, other parameters being equal, to take account of the role of Ca²⁺ in FPN1-mediated metal efflux. Both simulations (Na⁺/Ca²⁺) were performed in absence of iron, for which the binding site remained to be explored at the experimental level in the outward-facing conformation. The results of the 2 simulations were quite similar, especially regarding the bond network analyzed here (Supplemental Fig. S3). Na⁺ ions, however, fluctuated, whereas several Ca²⁺ ions were trapped in some regions during simulation, one of them artifactually interacting with a carboxyl group (Lys236) introduced after the truncation of the protein after the N-terminal domain. However, it is worth noting, that

overestimated binding affinities of divalent ions are a known problem in classic force fields (24).

Plasmid constructs

The wild-type (WT) FPN1-V5/CD8 bicistronic plasmid construct was generated by cloning full-length human *SLC40A1* and CD8 cDNA (Genbank: NM_0414585.5 and NM_001145873.1) into the pIRES2 DsRed-Express2 vector (Clontech Laboratories, Mountain View, CA, USA); the DsRed-Express2 fluorescent protein coding sequence was removed and replaced by CD8 cDNA, whereas a V5 epitope tag (GKPIPPLLGLDST) was introduced in the fifth extracellular loop of FPN1 to facilitate detection on flow cytometry. Iron release measurement used a pcDNA3.1-FPN1-V5(C-ter) construct (7). All ferroportin mutations were introduced in the pIRES_FPN1-V5_CD8 and pcDNA3.1_FPN1-V5 vectors using the QuickChange Site-Directed mutagenesis kit, according to the manufacturer's instructions (Agilent Technologies, Santa Clara, CA, USA). Sequencing analyses were performed to check the integrity of all plasmid constructs (full-length *SLC40A1* cDNA sequenced after each site-directed mutagenesis).

Culture and transfection of human epithelial kidney 293T cells

Human epithelial kidney (HEK)293T cells, from the American Type Culture Collection (Manassas, VA, USA), were incubated at 37°C in a 5% CO₂ humidified atmosphere and propagated in DMEM (Lonza, Basel, Switzerland) supplemented with 10% fetal bovine serum. Cells were transiently transfected using JetPEI (Polyplus, Illkirch-Graffenstaden, France), according to the manufacturer's instructions, and a 2:1 transfection reagent (μl)/plasmid DNA ratio (μg).

Flow cytometry

HEK293T cells (1.9×10^5 cells/well in 12-well plates) transfected with the pIRES_FPN1-V5_CD8 constructs were harvested with trypsin 36 h after transfection. Samples were pelleted (500 g, 5 min) and resuspended in PBS (pH 7.4) containing 1 mM EDTA and 10% fetal bovine serum, before being incubated for 30 min at 4°C with anti-V5-FITC (Thermo Fisher Scientific, Waltham, MA, USA) and anti-CD8-APC (Miltenyi Biotec, Bergisch Gladbach, Germany). Stained cells were pelleted (500 g, 5 min, 4°C) and resuspended in 400 μl PBS-EDTA. Cells were analyzed using a BD Accuri C6 flow cytometer [Becton Dickinson (BD), San Diego, CA, USA] and Flowlogic software (Miltenyi Biotec). Events were gated to exclude cell debris and aggregates, and to select cells with the desired levels of CD8 and FPN1-V5 expression; the windows were set up to exclude CD8- or FPN1-V5-negative cells (using mock-transfected cells as control), as well as cells with very high fluorescent intensity.

Intracellular ⁵⁵Fe measurements

⁵⁵Fe loading of human apotransferrin was performed as previously described (25). HEK293T cells (1.7×10^5 cells/well in 12-well plates) were transfected with WT or mutated pcDNA3.1_FPN1-V5 constructs for 24 h, before being cultured in Pro293a-CDM serum-free medium (Lonza) and preloaded with 20 μg/ml ⁵⁵Fe-transferrin for 16 h. Each pcDNA3.1_FPN1-V5 construct was codelivered with the pSV-β-galactosidase (β-gal) vector (Promega, Madison, WI, USA). Cells were harvested with trypsin, mixed with liquid scintillation fluid (Ultima Gold MV; Perkin-Elmer, Waltham, MA, USA) and counted for 2 min in a

TRI-CARB 1600 CA scintillation counter (PerkinElmer). ⁵⁵Fe radioactivity was normalized on total protein content and β-gal activity.

Statistical analysis

Data are presented as means (column bars) + sd. Comparisons used 2-tailed Student's *t* tests.

RESULTS

Model of the 3D structure of the outward-facing conformation of human FPN1

As previously reported (15), a model of the 3D structure of human FPN1 in an outward-facing conformation was built using the BbFpn structure (Bd2019; Protein Data Bank 5AYM) as template (see Materials and Methods). On the intracellular side (cytoplasmic gate), TM2, TM3, TM4, and TM5 (N-domain) interact tightly with TM10 and TM11 (C-domain) (Fig. 1A). Human FPN1 conserves the amino acid atoms thought to play a critical role in the BbFpn cytoplasmic gate (12). Asp157 (TM4, *BbFpn Asp140*) forms salt bridges with Arg88 (TM3, *BbFpn Arg73*) and Arg489 (TM11, *BbFpn Arg371*), whereas Arg88 also forms a salt bridge with Glu486 (preceding TM11, *BbFpn Glu368*) (Fig. 1A, green box at right). This network is completed with that provided by H-bonds formed, on the one hand, between the side-chain oxygens of Asp84 (TM2, *BbFpn Asp69*) and the main-chain nitrogen atoms of Gly490 and Ile491 (TM11) (*BbFpn Gly372 and Glu373*) (Fig. 1A, green box at right) and, on the other hand, between the side chains of Asn174 (TM5, *BbFpn Asn155*) and Gln481 (TM10, *BbFpn Gln363*) (Fig. 1A, orange box at left). The previously reported salt bridge between Arg178 and Asp473 also participates in this network (15).

A simplified view of the interdomain and intradomain interactions for both the bacterial and the human iron exporter is provided in Supplemental Fig. S1.

In vitro evaluation of 7 candidate gating residues

To experimentally test the 3D model for the intracellular gate, we individually mutagenized Arg88, Asp157, Glu486, Arg489, Asp84, and Gln481 to Ala. Ala is the second smallest amino acid after Gly. This nonpolar amino acid has the highest propensity of all 20 natural amino acids for the α-helical state (26). The selected Ala substitutions were thus likely to have limited impact on local human FPN1 structure. Only Asn174 was mutated to isoleucine, as the p.Asn174Ile missense mutation was previously proved to be defective for iron egress while being normally addressed to the cell surface (7, 27).

A bicistronic construct was used to evaluate the concurrent plasma membrane expression of human FPN1 (conjugated with a V5 epitope) and CD8 on flow cytometry. Taking account of the level of CD8 in HEK293T cells, which do not normally express this membrane protein, enabled correction for differences in transfection efficiency

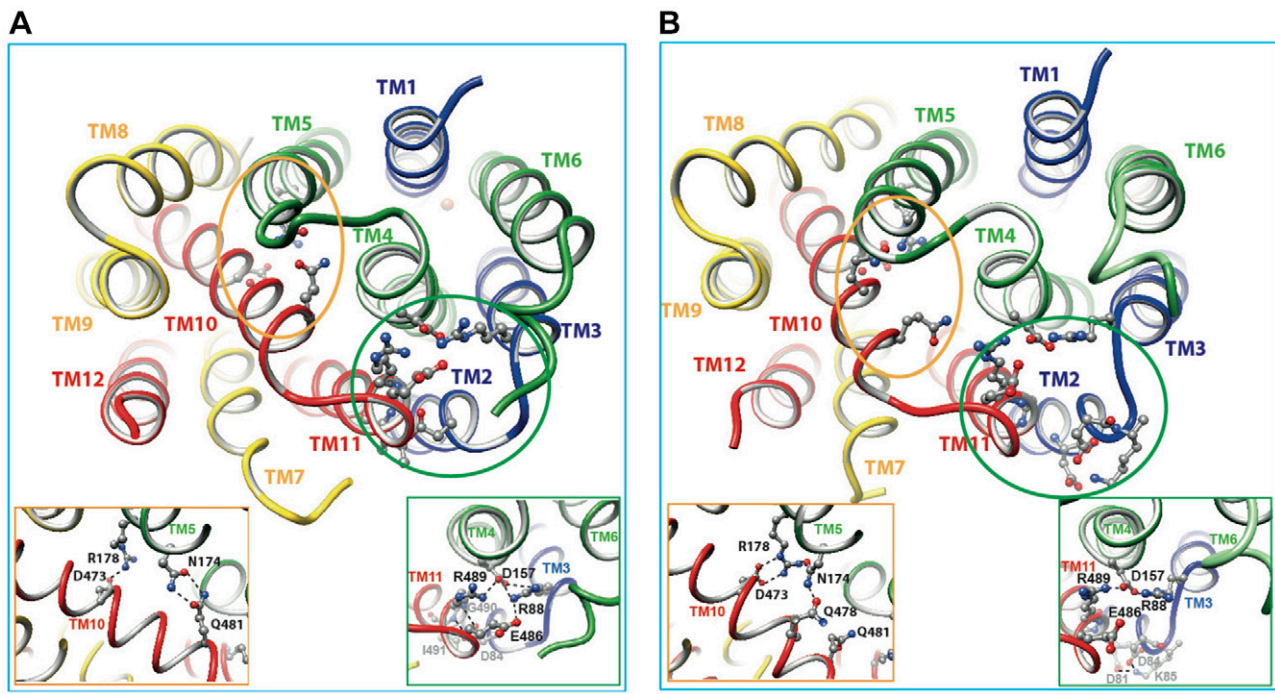


Figure 1. Model of the 3D structure of the human FPN1 cytoplasmic gate. Before (0-ns) (A) and after (100-ns) (B) MD simulation. The 3D structure is shown in a ribbon representation, with amino acids involved in salt bridges or H-bonds depicted in a ball-and-stick representation. TM helices are labeled and colored (TM1–TM3: blue, TM4–TM6: green, TM7–TM9: yellow, TM10–TM12: red). This figure was drawn using chimera. For convenience, amino acids are described by a 1-letter code, instead of the 3-letter code used in the main text.

between samples. The p.Ala77Asp missense mutation, which significantly damages FPN1 structure and is known to prevent cell surface localization, was used as negative control. It was noteworthy that expression of FPN1-V5 fusion proteins was lower than the CD8 control in all analyzed cell populations (cells expressing WT FPN1-V5 fusion displayed >40% reduction); this suggests differences in the levels of FPN1 and CD8 translation initiated from the bicistronic mRNA. An important difference was observed in the proportions of FPN1-WT⁺/CD8⁺ and FPN1-A77D⁺/CD8 cells ($P < 0.001$), confirming that the p.Ala77Asp mutant causes FPN1 mislocalization (Fig. 2A). Expression of the p.Asp84Ala mutant also differed significantly from the WT protein ($P < 0.05$). The other 6 variants reached the plasma membrane correctly.

Radioactively labeled iron accumulation was measured in HEK293T cells transiently transfected with pcDNA3.1 plasmids encoding FPN1-V5 fusion proteins, using cells transfected with the commercial pcDNA3.1-V5-His empty vector as control. pcDNA3.1 plasmids were codelivered with a normalization vector encoding the β -gal enzyme. A total of 24 h after transfection, HEK293T cells were cultured in serum-free medium and preloaded with 20 $\mu\text{g/ml}$ ^{55}Fe -transferrin for 16 h. The cell lysates were assayed for ^{55}Fe quantity, β -gal activity (to correct for differences in transfection efficiency) and total protein concentration (to correct for differences in final cell number). As shown in Fig. 2B, cells transfected with the WT FPN1-V5 fusion protein displayed 2- to 3-fold lower iron accumulation. The p.Arg88Ala, p.Asp157Ala, p.Arg489Ala, p.Asp84Ala, and p.Asn174Ile mutants were not able to

export ^{55}Fe iron in amounts comparable with WT FPN1. Two mutants, p.Gln481Ala and p.Glu486Ala, retained their ability to export iron out of the cell.

Taken together, the results shown in Fig. 2A, B demonstrate that Arg88, Asp157, Arg489, and Asn174 are important for iron export. In contrast, Gln481 and Glu486 can be changed to Ala without altering FPN1 function. In the light of this, we then investigated the function of the p.Gln481Ala-Glu486Ala double mutant. Figure 3A, B shows that it localized to the cell surface in the same way as the WT protein and that it retained export function.

MD simulations

To further understand the differences observed for the mutants tested, molecular dynamics simulations were run on the human FPN1 3D structure model in an appropriate environment (Materials and Methods). Root mean square deviations for the protein backbone during 100-ns MD simulation were calculated relative to the coordinates of the initial structures (Supplemental Fig. S2). More constant values were observed from 20 to 25 ns onward, after an initial 10-ns fast-rise region, indicating that the model structure had reached conformation steady state.

Comparing conformations in this steady state (illustrated here at 100 ns; Fig. 1B) to the initial 3D structure (0 ns; Fig. 1A) revealed a slight reorganization of the intracellular gate bond network. Although the salt bridges between Asp157 and Arg88 and Asp157 and Arg489 appeared very stable throughout the simulation, as assessed by monitoring the distances between the

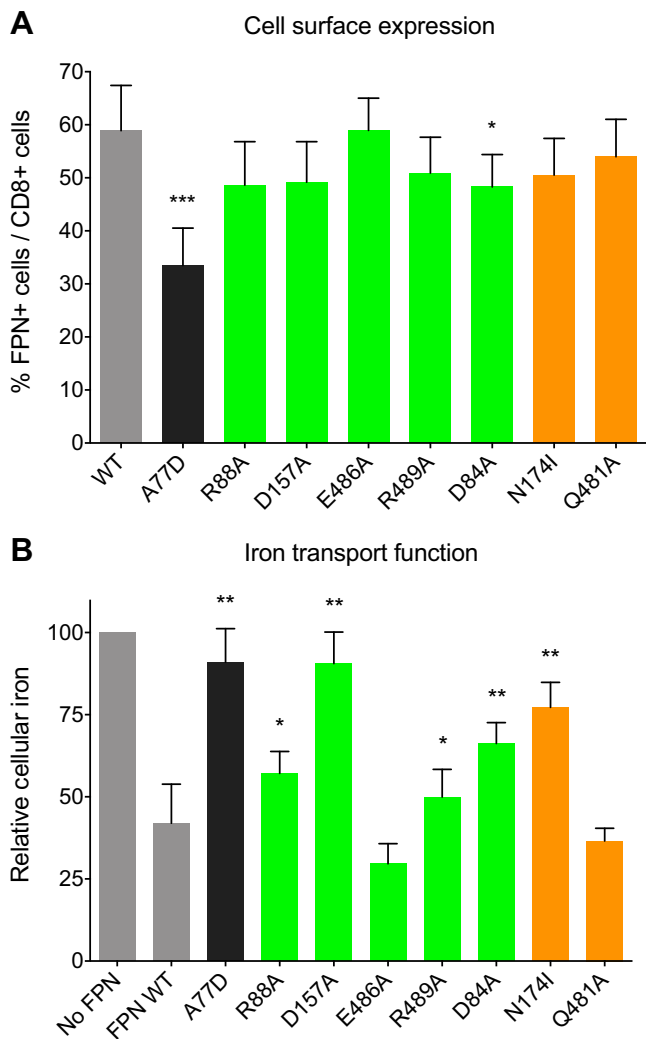


Figure 2. Effect on cell surface expression and iron export of Ala or isoleucine substitutions for amino acids predicted to be involved in interactions between the N- and the C-lobe of human FPN1 in the outward-facing state. Green bars indicate residues predicted to form salt bridges or hydrogen bonds between helices 2, 3, 4, and 11. Orange bars indicate residues predicted to form a hydrogen bond between helices 5 and 10. For convenience, amino acids are described by a 1-letter code, instead of the 3-letter code used in the main text. **A)** HEK293T cells were transiently transfected with the bicistronic pIRES2 plasmid encoding both full-length human FPN1 and CD8. A 14-aa V5 epitope (Gly-Lys-Pro-Ile-Pro-Asn-Pro-Leu-Leu-Gly-Leu-Asp-Ser-Thr) was inserted in the fifth extracellular loop of FPN1 to allow plasma membrane detection. After 36 h, cells were double-stained for CD8 (APC) and the FPN1-V5 fusion protein (FITC) and analyzed by 2-color flow cytometry. Data are presented as percentages of FPN1-positive over CD8-positive events. Each bar represents the means \pm SD of 6 independent experiments. *P* values were calculated by a Student's *t* test. **P* < 0.05, ****P* < 0.001. **B)** HEK293T cells were transfected with pcDNA3.1-FPN1-V5-His vectors, grown for 24 h, and then fed with 20 μ g/ml 55 Fe-transferrin for 16 h. Cells were then washed and counted. Counts per minute (cpm) were normalized by total protein and β -gal activity. Empty vector (No FPN) samples taken as 100% values generally achieved 1000–2500 cpm. Each bar represents the means \pm SD of 5 independent experiments. *P* values were calculated by a Student's *t* test. **P* < 0.05, ***P* < 0.01 compared with WT FPN1.

involved atoms (Fig. 4A), Glu486 moved away, with its 2 side-chain oxygen atoms usually free from any interaction. Interestingly, the 2 H-bonds between Asp84 and the main-chain N atoms of Gly490 and Ile491 were rapidly lost and only occasionally reformed (Fig. 4B), whereas one of the side-chain oxygen atoms of Asp84 was able to form a salt bridge with Lys85, itself bound to Asp81 (Fig. 4C). This double salt bridge was not constant throughout the simulation, with variable positions of Lys85 side-chain and transient H-bonds of Asp84 with Gly490 and Ile491 main-chain N atoms, suggesting that this feature may be a key-point for conformational change during the human FPN1 cycle. It was noteworthy that these bonds could not be formed in the BbFpn structure because the amino acids homologous to Asp81 and Lys85 are Lys66 and Thr70,

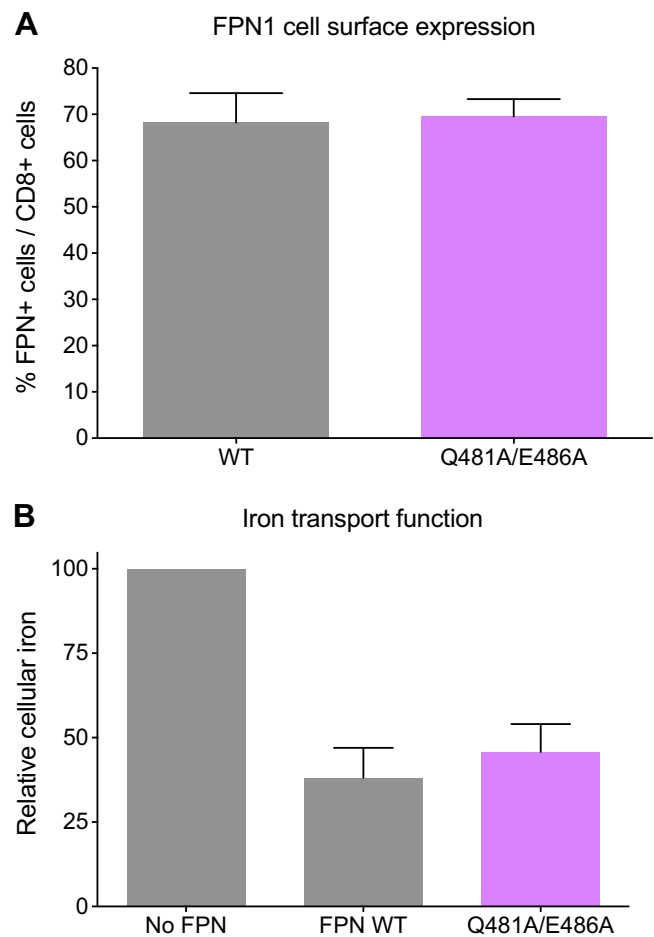


Figure 3. Cell surface expression and iron export ability of the Gln481Ala-Glu486Ala double mutant. **A)** HEK293T cells were transiently transfected with the bicistronic pIRES2 plasmid encoding both full-length human FPN1 and CD8. After 36 h, cells were double-stained for CD8 (APC) and the FPN1-V5 fusion protein (FITC) and analyzed by 2-color flow cytometry. Data are presented as percentages of FPN1-positive over CD8-positive events. Each bar represents the means \pm SD of 4 independent experiments. **B)** HEK293T cells were transfected with pcDNA3.1-FPN1-V5-His vectors, grown for 24 h, and then fed with 20 μ g/ml of 55 Fe-transferrin for 16 h. Cells were then washed and counted. Counts per minute (cpm) were normalized by total protein and β -gal activity. Each bar represents the means \pm SD of 5 independent experiments.

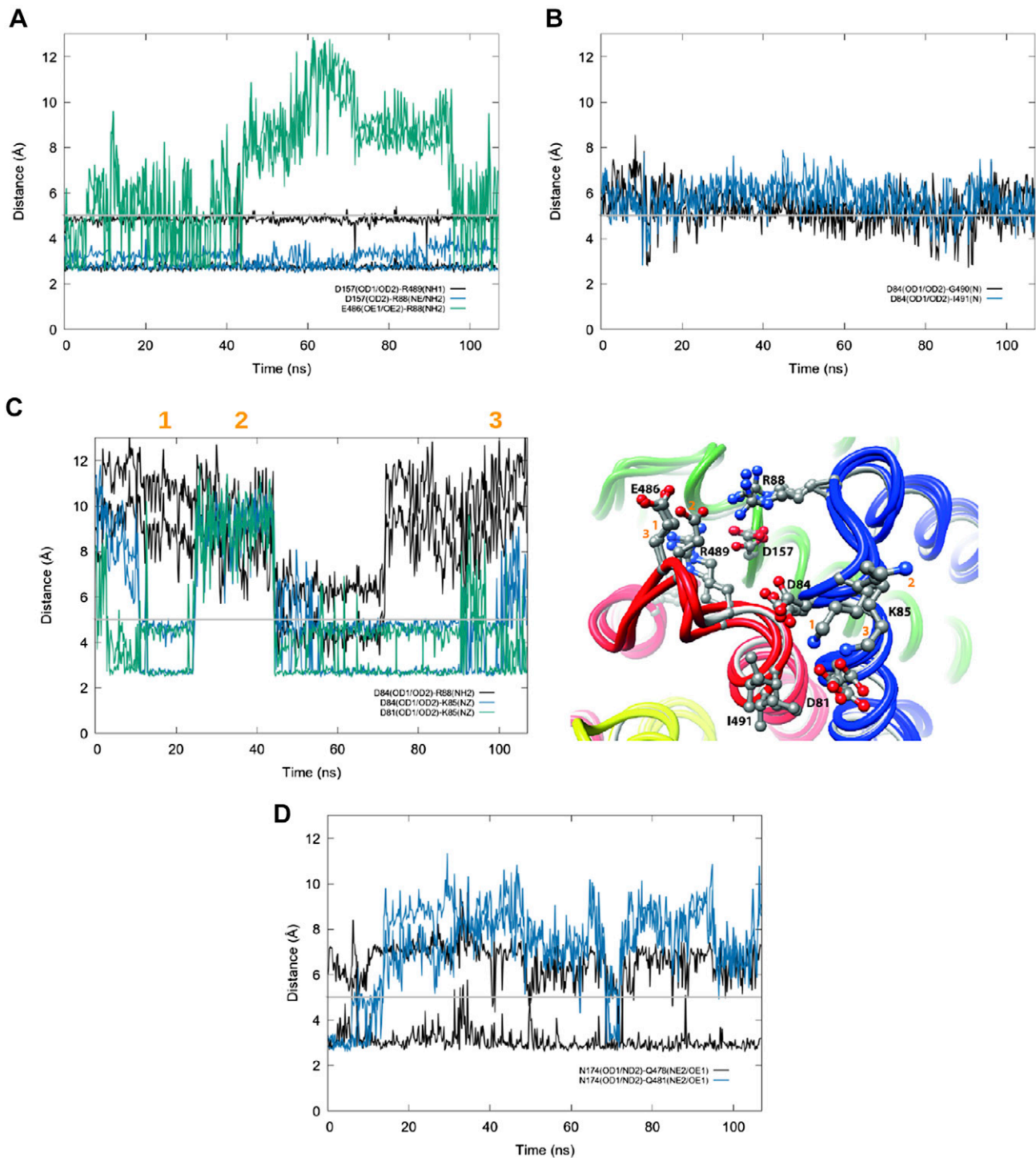


Figure 4. Evolution, along the MD simulation, of the distances between atoms involved in noncovalent bonds. Distances were plotted (using gnuplot) as a function of trajectory time between pairs of atoms (N, OD1, OD2, OE1, OE2, ND2, NE1, NH1, NH2, NZ), which may be involved in noncovalent bonds and are reported here considering the groups depicted in Fig. 1. The distance of 5 Å (horizontal gray line) is indicated as a reference, below which bonds can be observed. *A–C*) Green box of Fig. 1: interhelical side-chain–side-chain interactions involving TM3 (Arg88), TM4 (Asp157), and TM11 (Glu486, Arg489) (*A*); interhelical side-chain–main-chain interactions involving oxygen atoms (OD1/OD2) of the side chain of Asp84 and the nitrogen main-chain atom (N) of Gly490 and Ile491 (*B*); intrahelical side-chain–side-chain interactions at the level of TM2 involving Asp84, Lys85, Asp88, and Arg88 (*C*). At right are represented 3 different conformational states extracted from the simulation, illustrating different positions of the side chains of Glu486 and Lys85. *D*) Orange box of Fig. 1: interhelical side-chain–side-chain interactions involving TM5 (Asn174) and TM10 (Gln478 and Gln481). The inset between panels *C* and *D* represents 3 different conformational states extracted from the simulation, illustrating different positions of the side chains of Glu486 and Lys85. This figure was drawn using chimera (54). For convenience, amino acids are described by a 1-letter code, instead of the 3-letter code used in the main text.

respectively. Finally, the H bond between Gln481 and Asn174 was also not maintained, and it occurred very rarely during the simulation (Fig. 4D). In contrast, Asn174 made other H-bonds with Gln478 on TM10 and Arg178 on TM5, Arg178 also forming an interlobe salt bridge with Asp473, as previously reported (15).

In conclusion, these results explain the noncritical role of Gln481 and Glu486 for the FPN1 function, highlight an alternative functional role of Asp84 in a dynamic network, and suggest a critical role for Gln478, interacting with Asn174, itself included in a wide bond network involving Arg178 and Asp473. These 3 features were not anticipated from the experimental static 3D structure of BbFpn.

In vitro evaluation of the Gln478Ala mutant

To check our predictions, we also evaluated the effects of the Gln478Ala mutant. The mutant was detected on the surface of HEK293T transiently transfected cells at levels similar to those seen with the WT protein (Fig. 5A). Its ability to export iron out the cell was, however, markedly reduced (Fig. 5B). Of note, functional consequences of the Gln478Ala mutant were comparable to those observed for the Asn174Ile mutant (Fig. 2A, B).

Genotype-phenotype correlations

Based on the literature, we identified 13 missense mutations that affect 7 different gating residues (Asp84, Arg88, Asp157, Asn174, Arg178, Arg489, and Gly490) and have been reported in a total of 77 patients (32 female, 45 male; Table 1). As summarized in Fig. 6, most patients presented serum ferritin >1000 $\mu\text{g/L}$ and transferrin saturation <50% (females) or <60% (males) at diagnosis. This is characteristic of the hemochromatosis type 4A subtype and FPN1 loss-of-function (28, 29).

DISCUSSION

In-depth knowledge of the main elements of normal FPN1 physiology is an important prerequisite for understanding the mechanism of iron export in mammals. Here, we investigated the structure-function relationships of a set of amino acids previously predicted, from the bacterial homolog BbFpn 3D structure, as key elements for stabilizing the protein in the outward-facing state. This revealed non-covalent interactions between several amino acids that are conserved between species and form a first essential interaction network. Moreover, MD simulations performed on the model of the human FPN1 3D structure led to explain the noncritical role of a few amino acids and to reveal other critical ones, which were further supported at the experimental level. These additional residues are also permanently involved in noncovalent interactions, with either a unique or multiple partners, within networks that are specific to human FPN1. This study thus provides for the first time an accurate topological description of the human FPN1 intracellular gate.

MFS transporters must undergo large conformational changes to transport substrates across membranes through

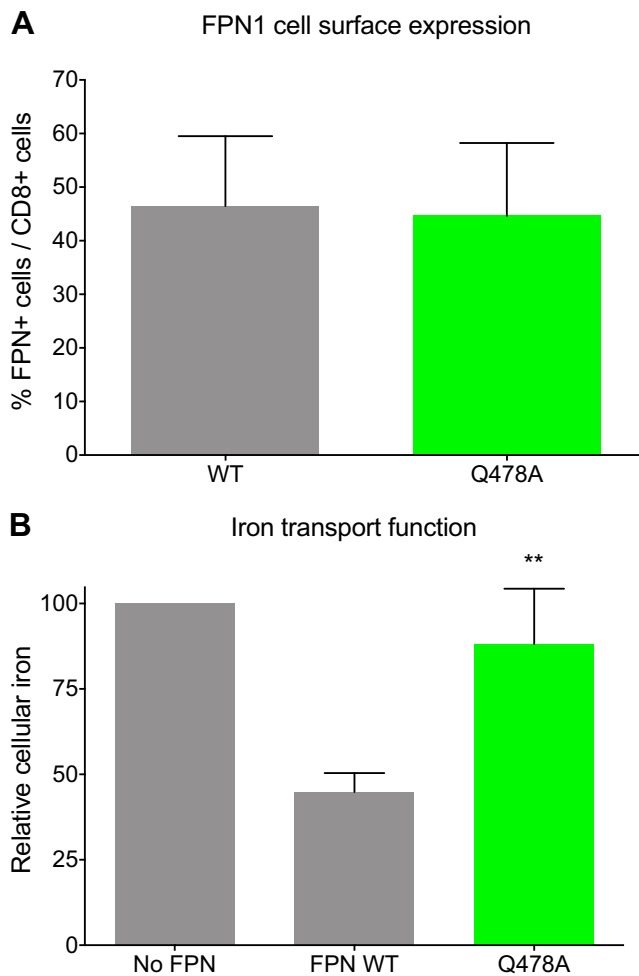


Figure 5. Cell surface expression and iron export ability of the Gln478Ala mutant. *A*) HEK293T cells were transiently transfected with the bicistronic pIRES2 plasmid encoding both full-length human FPN1 and CD8. After 36 h, cells were double-stained for CD8 (APC) and the FPN1-V5 fusion protein (FITC) and analyzed by 2-color flow cytometry. Data are presented as percentages of FPN1-positive over CD8-positive events. Each bar represents the means \pm SD of 3 independent experiments. *B*) HEK293T cells were transfected with pcDNA3.1-FPN1-V5-His vectors, grown for 24 h, and then fed with 20 $\mu\text{g/ml}$ of ^{55}Fe -transferrin for 16 h. Cells were then washed and counted. Counts per minute (cpm) were normalized by total protein and β -gal activity. Each bar represents the means \pm SD of 5 independent experiments. *P* values were calculated by a Student's *t* test. ***P* < 0.01 compared with WT FPN1.

alternate access mechanism. Accordingly, gates are found at each end of the protein, which open and lock in concert to allow passage of substrates. Gating residues comprise amino acids that mediate interactions between the N- and C- domains in 1 conformational state. Such contacts are important not only for stabilizing the different conformational states but also for ensuring cooperation in conformational changes, preventing forbidden states with both gates open (10). Gating residues in MFS proteins often involve charged residues forming salt bridges (30, 31), but this appears to be a recurrent feature of several membrane systems (32). Salt bridges can also be found in the central cavities of

TABLE 1. List of mutations in the *SLC40A1* gene that affect an FPN1 gating residue

Mutation	Gender	Age at diagnosis (yr)	Reference
p.Asp84Glu	Female (<i>n</i> = 1)	26	40
p.Arg88Thr	Female (<i>n</i> = 1)	18	41
p.Arg88Gly	Male (<i>n</i> = 6)	15–61	38, 42
	Female (<i>n</i> = 2)	41–77	
p.Asp157Ala	Male (<i>n</i> = 2)	38–41	43–46, 48
	Female (<i>n</i> = 2)	Not provided	
p.Asp157Gly	Male (<i>n</i> = 5)	58–66	38, 47
	Female (<i>n</i> = 2)	42–66	
p.Asp157Asn	Male (<i>n</i> = 2)	61–64	36, 49
	Female (<i>n</i> = 4)	22–76	
p.Asp157Tyr	Male (<i>n</i> = 1)	20	38
	Female (<i>n</i> = 2)	64	
p.Asn174Ile	Female (<i>n</i> = 2)	38–66	27, 50
	Male (<i>n</i> = 1)	45	
p.Arg178Gln	Female (<i>n</i> = 8)	11–72	15, 42, 51
	Male (<i>n</i> = 17)	6–71	
p.Arg489Lys	Female (<i>n</i> = 4)	39–60	39
	Male (<i>n</i> = 2)	28–54	
p.Arg489Ser	Male (<i>n</i> = 4)	43–81	45, 52
	Female (<i>n</i> = 4)	23–54	
p.Gly490Asp	Male (<i>n</i> = 3)	31–47	38, 53
	Female (<i>n</i> = 2)	27–71	
p.Gly490Ser	Female (<i>n</i> = 2)	27–71	38, 42
	Male (<i>n</i> = 1)	24	

membrane domains, stabilizing specific conformations (17, 33). The 3D structure of BbFpn suggests that the intra- and extracellular gates clearly differ, involving salt bridge or H-bonds and hydrophobic contacts, respectively (12).

Investigating both the 3D structure of human FPN1 and the cellular effects of Ala-substituted mutants (Figs. 1 and 2) confirmed the existence of salt bridges between Arg88 (TM3), Asp157 (TM4), and Arg489 (TM11). These electrostatic interactions, involving conserved residues and appearing very stable along MD simulations (Supplemental Fig. S3A), are completed by another interdomain salt bridge between Arg178 (TM5) and Asp473 (TM10), as we demonstrated very recently (15). Interestingly, this last salt bridge appears specific to human FPN1; it cannot exist in the BbFpn structure because the residue equivalent to Asp473 is Ser355. The whole salt-bridge network described

here is likely very important for stabilization of human FPN1 in the outward-open conformation.

An intriguing issue was the observation that Gln481 (TM10) and Glu486 (preceding TM11), which were predicted from the BpFpn structure (corresponding amino acids Gln363 and Glu368) as also involved in the intracellular gate, are not essential to human FPN1 activity. These observations were reinforced by the study of the Gln481Ala-Glu486Ala double mutant, which was indistinguishable from the WT protein for cell surface expression and iron export ability (Fig. 3). This marks a clear difference from hypotheses based on the bacterial homolog outward-facing structure, and this can only be explained after MD simulations and refinement of the model of the 3D structure of human FPN1. Hence, Gln481 is thought to interact only transiently with Asn174 (TM5),

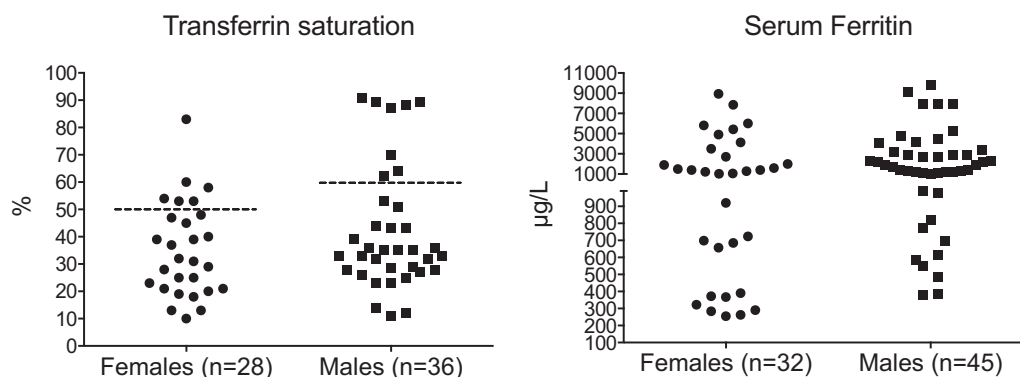


Figure 6. Distribution of iron parameters among suspected hemochromatosis type 4A patients with a missense mutation affecting an FPN1 gating residue. Serum ferritin and transferrin saturation (when available) values were extracted from the literature for 11 missense mutations (listed in Table 1) and 67 patients. Data are presented by gender because penetrance of the hemochromatosis type 4A-related genotypes at the *SLC40A1* locus are known to be lower in females.

which actually forms quasi-stable H-bonds with both Gln478 (TM10) and Arg178 (TM5) (Figs. 1 and 4). The 2 side-chain oxygen atoms in Glu486 are very often free of any interaction (Figs. 1 and 4A), and Glu486 is thus unable to actively participate in the interaction network formed by Arg88, Asp157, and Arg489. The situation of Asp84 is even more complex because it relies on local interactions that do not exist in the bacterial homolog BbFpn. Indeed, Asp84 is expected to briefly form H-bonds with both the main-chain N atoms of Gly490 and Ile491, when not forming a salt bridge with Lys85. The local network involving Asp84 and Lys85 in TM2 can be reinforced by an additional bond between Lys85 and Asp81 (Figs. 1 and 4B–D). Important conclusions to our study, which are supported at the experimental level, are thus the identification of Gln478 as an additional critical actor of the human FPN1 intracellular gate and of the involvement of Asn174 and Asp84 in multiple bonds also playing a fundamental role in this gate. Interestingly, these networks of interactions involve residues that are specific to human FPN1: Asp473, Gln478, Asp81, and Lys85 (Ser355, Glu360, Lys66, and Thr70, respectively, in BbFpn).

Worth noting is the potential role that surrounding phospholipids may play in the structural rearrangements enabling alternate access mechanism by interfering with the conserved network of interactions in the cytoplasmic gate. In particular, phosphatidylethanolamine lipids may directly interact with some acidic residues of the intracellular gate charged network, such as Asp84, and stabilize the inward-facing conformation by interfering with contacts between the cytoplasmic ends of the N- and C-lobe. The role of such molecular switches in the dynamic interconversion underpinning transport cycle has been described for some other MFS transporters (34, 35); it should be further investigated in the particular case of FPN1.

Like other adult-onset autosomal dominant diseases, hemochromatosis type 4A (or ferroportin disease) is characterized by incomplete penetrance and wide phenotypic heterogeneity. So far, 51 missense mutations have been associated with the disease (28, 36, 37). Not all have been functionally investigated, and not all have been definitively identified as disease-causing. It is, however, interesting that 13 missense mutations map to the FPN1 intracellular gate. They correspond to 7 gating residues (Asp84, Arg88, Asp157, Asn174, Arg178, Arg489, and Gly490) that, according to our investigations, are involved in the formation of noncovalent interactions at the interface between the N- and the C-domains (Fig. 1). As illustrated in Fig. 6, patients with these missense mutations generally present high serum ferritin concentrations ($>1000 \mu\text{g/L}$), suggesting significant iron overload in tissue, related to serious FPN1 dysfunction. The p.Asp157Gly, p.Asp157Tyr, and p.Arg489Lys substitutions are known to cause FPN1 mislocalization (38, 39). This likely results from folding defects in TM helices 2, 4, or 11 or local unstability of the structure, or any combination thereof. By contrast, the p.Arg88Gly, p.Asp157Ala, p.Asn174Ile, and p.Arg178Gln substitutions reduce the ability of FPN1 to export iron without defective cell surface expression (7, 15, 27). This is now explained by the loss of interdomain interactions in the outwardly oriented FPN1 state. The p.Arg88Thr, p.Asp157Asn, and p.Arg489Ser substitutions have not yet been studied

experimentally; in light of the above observations, however, it can reasonably be anticipated that they are all deleterious.

In summary, the present study provides an unprecedented view of the interactions needed to form and stabilize the FPN1 intracellular gate. It highlights intra- and interdomain interactions, some of which are not existing in the bacterial homolog BbFpn, thus identifying the fundamental role of a set of specific residues in the iron transport cycle in humans. It also confirms that hemochromatosis type 4A is not restricted to missense mutations that cause protein mislocalization, thus increasing our ability to interpret rare genetic variants at the *SLC40A1* locus. This will have profound implications for patient management. More extensive MD simulations are warranted to understand the mechanisms associated with the conformational changes leading to the inward-facing conformation and the influence of iron and calcium binding and release. Particular attention should also be paid to the identification of hydrophobic interdomain interactions in the inward-facing structure of FPN1. This is necessary in order to identify the entire network of gating residues that participate in the global transition from the outward-facing to the inward-facing state and *vice versa* (36, 40–53). FJ

ACKNOWLEDGMENTS

The authors thank George Gao and Alain R.M. Townsend (Weatherall Institute, Oxford University, Oxford, United Kingdom) for the generous gift of the CD8 expression vector. The protocol used for molecular dynamics simulation was developed during the research work on the Cystic Fibrosis Transmembrane Conductance Regulator (CFTR) protein, which was supported by the French Association “Vaincre La Mucoviscidose,” and performed using High-Performance Computing (HPC) resources from Grand Equipement National de Calcul Intensif (GENCI)/Centre Informatique National de l’Enseignement Supérieur (CINES) (Grants 2017-A0020707206, 2018-A0040707206, and 2019-A0060707206). This work was also supported by grants from the French Hospital Clinical Research Program (Programme Hospitalier de Recherche Clinique 2009; Brest University Hospital; UF0857), the Gaetan Saleun Association, and the Laboratory of Excellence (GR-Ex) (ANR-11-LABX-0051). The labex GR-Ex is funded by the Investissement D’avenir d’Excellence (IdEx) program “Investissements d’avenir” of the French National Research Agency (ANR-18-IDEX-0001). The authors declare no conflicts of interest.

AUTHOR CONTRIBUTIONS

J. Guellec, A. Elbahnsi, M. Le Tertre, K. Uguen, I. Gourlaouen, and I. Callebaut conducted experiments; C. Férec, C. Ka, I. Callebaut, and G. Le Gac analyzed data; I. Callebaut and G. Le Gac designed the study and wrote the manuscript; and all authors contributed to the editing of the final manuscript.

REFERENCES

1. Anderson, G. J., and Frazer, D. M. (2017) Current understanding of iron homeostasis. *Am. J. Clin. Nutr.* **106**(Suppl 6), 1559S–1566S
2. Drakesmith, H., Nemeth, E., and Ganz, T. (2015) Ironing out ferroportin. *Cell Metab.* **22**, 777–787

3. Hentze, M. W., Muckenthaler, M. U., Galy, B., and Camaschella, C. (2010) Two to tango: regulation of Mammalian iron metabolism. *Cell* **142**, 24–38
4. Donovan, A., Lima, C. A., Pinkus, J. L., Pinkus, G. S., Zon, L. I., Robine, S., and Andrews, N. C. (2005) The iron exporter ferroportin/Slc40a1 is essential for iron homeostasis. *Cell Metab.* **1**, 191–200
5. Nemeth, E., Tuttle, M. S., Powelson, J., Vaughn, M. B., Donovan, A., Ward, D. M., Ganz, T., and Kaplan, J. (2004) Hepcidin regulates cellular iron efflux by binding to ferroportin and inducing its internalization. *Science* **306**, 2090–2093
6. Girelli, D., Nemeth, E., and Swinkels, D. W. (2016) Hepcidin in the diagnosis of iron disorders. *Blood* **127**, 2809–2813
7. Le Gac, G., Ka, C., Joubrel, R., Gourlaouen, I., Lehn, P., Mornon, J.-P., Férec, C., and Callebaut, I. (2013) Structure-function analysis of the human ferroportin iron exporter (SLC40A1): effect of hemochromatosis type 4 disease mutations and identification of critical residues. *Hum. Mutat.* **34**, 1371–1380
8. Wallace, D. F., Harris, J. M., and Subramaniam, V. N. (2010) Functional analysis and theoretical modeling of ferroportin reveals clustering of mutations according to phenotype. *Am. J. Physiol. Cell Physiol.* **298**, C75–C84
9. Bonaccorsi di Patti, M. C., Polticelli, F., Cece, G., Cutone, A., Felici, F., Persichini, T., and Musci, G. (2014) A structural model of human ferroportin and of its iron binding site. *FEBS J.* **281**, 2851–2860
10. Quistgaard, E. M., Löw, C., Guettou, F., and Nordlund, P. (2016) Understanding transport by the major facilitator superfamily (MFS): structures pave the way. *Nat. Rev. Mol. Cell Biol.* **17**, 123–132
11. Bonaccorsi di Patti, M. C., Polticelli, F., Tortosa, V., Furbetta, P. A., and Musci, G. (2015) A bacterial homologue of the human iron exporter ferroportin. *FEBS Lett.* **589**, 3829–3835
12. Taniguchi, R., Kato, H. E., Font, J., Deshpande, C. N., Wada, M., Ito, K., Ishitani, R., Jormakka, M., and Nureki, O. (2015) Outward- and inward-facing structures of a putative bacterial transition-metal transporter with homology to ferroportin. *Nat. Commun.* **6**, 8545
13. Deshpande, C. N., Ruwe, T. A., Shawki, A., Xin, V., Vieth, K. R., Valore, E. V., Qjao, B., Ganz, T., Nemeth, E., Mackenzie, B., and Jormakka, M. (2018) Calcium is an essential cofactor for metal efflux by the ferroportin transporter family. *Nat. Commun.* **9**, 3075
14. Jardetzky, O. (1966) Simple allosteric model for membrane pumps. *Nature* **211**, 969–970
15. Ka, C., Guellec, J., Pepermans, X., Kannengiesser, C., Ged, C., Wuyts, W., Cassiman, D., de Ledinghen, V., Varet, B., de Kerguenec, C., Oudin, C., Gourlaouen, I., Lefebvre, T., Férec, C., Callebaut, I., and Le Gac, G. (2018) The *SLC40A1*R178Q mutation is a recurrent cause of hemochromatosis and is associated with a novel pathogenic mechanism. *Haematologica* **103**, 1796–1805
16. Webb, B., and Sali, A. (2017) Protein structure modeling with MODELLER. *Methods Mol. Biol.* **1654**, 39–54
17. Hoffmann, B., Elbahnsi, A., Lehn, P., Décout, J. L., Pietrucci, F., Mornon, J. P., and Callebaut, I. (2018) Combining theoretical and experimental data to decipher CFTR 3D structures and functions. *Cell. Mol. Life Sci.* **75**, 3829–3855
18. Lamoureux, G., and Roux, B. (2006) Absolute hydration free energy scale for alkali and halide ions established from simulations with a polarizable force field. *J. Phys. Chem. B* **110**, 3308–3322
19. Beglov, D., and Roux, B. (1994) Finite representation of an infinite bulk system: solvent boundary potential for computer simulations. *J. Chem. Phys.* **100**, 9050
20. Jorgensen, W. L., Chandrasekhar, J., Madura, J. D., Impey, R. W., and Klein, M. L. (1983) Comparison of simple potential functions for simulating liquid water. *J. Chem. Phys.* **79**, 926
21. Jo, S., Cheng, X., Lee, J., Kim, S., Park, S.-J., Patel, D. S., Beaven, A. H., Lee, K. I., Rui, H., Park, S., Lee, H. S., Roux, B., MacKerell, A. D., Jr., Klauda, J. B., Qi, Y., and Im, W. (2017) CHARMM-GUI 10 years for biomolecular modeling and simulation. *J. Comput. Chem.* **38**, 1114–1124
22. Hart, K., Foloppe, N., Baker, C. M., Denning, E. J., Nilsson, L., and Mackerell, A. D., Jr. (2012) Optimization of the CHARMM additive force field for DNA: improved treatment of the BI/BII conformational equilibrium. *J. Chem. Theory Comput.* **8**, 348–362
23. Phillips, J. C., Braun, R., Wang, W., Gumbart, J., Tajkhorshid, E., Villa, E., Chipot, C., Skeel, R. D., Kalé, L., and Schulten, K. (2005) Scalable molecular dynamics with NAMD. *J. Comput. Chem.* **26**, 1781–1802
24. Heinz, L. P., Kopec, W., de Groot, B. L., and Fink, R. H. A. (2018) *In silico* assessment of the conduction mechanism of the Ryanodine Receptor 1 reveals previously unknown exit pathways. *Sci. Rep.* **8**, 6886
25. Ka, C., Le Gac, G., Dupradeau, F.-Y., Rochette, J., and Férec, C. (2005) The Q283P amino-acid change in HFE leads to structural and functional consequences similar to those described for the mutated 282Y HFE protein. *Hum. Genet.* **117**, 467–475
26. Callebaut, I., Labesse, G., Durand, P., Poupon, A., Canard, L., Chomilier, J., Henrissat, B., and Mornon, J. P. (1997) Deciphering protein sequence information through hydrophobic cluster analysis (HCA): current status and perspectives. *Cell. Mol. Life Sci.* **53**, 621–645
27. De Domenico, I., McVey Ward, D., Nemeth, E., Ganz, T., Corradini, E., Ferrara, F., Musci, G., Pietrangelo, A., and Kaplan, J. (2006) Molecular and clinical correlates in iron overload associated with mutations in ferroportin. *Haematologica* **91**, 1092–1095
28. Pietrangelo, A. (2017) Ferroportin disease: pathogenesis, diagnosis and treatment. *Haematologica* **102**, 1972–1984
29. Vlasveld, L. T., and Swinkels, D. W. (2018) Loss-of-function ferroportin disease: novel mechanistic insights and unanswered questions. *Haematologica* **103**, 1753–1755
30. Fowler, P. W., Orwick-Rydmark, M., Radestock, S., Solcan, N., Dijkman, P. M., Lyons, J. A., Kwok, J., Caffrey, M., Watts, A., Forrest, L. R., and Newstead, S. (2015) Gating topology of the proton-coupled oligopeptide symporters. *Structure* **23**, 290–301
31. Solcan, N., Kwok, J., Fowler, P. W., Cameron, A. D., Drew, D., Iwata, S., and Newstead, S. (2012) Alternating access mechanism in the POT family of oligopeptide transporters. *EMBO J.* **31**, 3411–3421
32. Latorraca, N. R., Fastman, N. M., Venkatakrishnan, A. J., Frommer, W. B., Dror, R. O., and Feng, L. (2017) Mechanism of substrate translocation in an alternating access transporter. *Cell* **169**, 96–107.e12
33. Stelzl, L. S., Fowler, P. W., Sansom, M. S. P., and Beckstein, O. (2014) Flexible gates generate occluded intermediates in the transport cycle of LacY. *J. Mol. Biol.* **426**, 735–751
34. Martens, C., Shekhar, M., Borysik, A. J., Lau, A. M., Reading, E., Tajkhorshid, E., Booth, P. J., and Politis, A. (2018) Direct protein-lipid interactions shape the conformational landscape of secondary transporters. *Nat. Commun.* **9**, 4151
35. Corradi, V., Sejdiu, B. I., Mesa-Galoso, H., Abdizadeh, H., Noskov, S. Y., Marrink, S. J., and Tieleman, D. P. (2019) Emerging diversity in lipid-protein interactions. *Chem. Rev.* **119**, 5775–5848
36. Majore, S., Bonaccorsi di Patti, M. C., Valiante, M., Polticelli, F., Cortese, A., Di Bartolomeo, S., De Bernardo, C., De Muro, M., Faienza, F., Radio, F. C., Grammatico, P., and Musci, G. (2018) Characterization of three novel pathogenic SLC40A1 mutations and genotype/phenotype correlations in 7 Italian families with type 4 hereditary hemochromatosis. *Biochim. Biophys. Acta Mol. Basis Dis.* **1864**, 464–470
37. Wang, Y., Du, Y., Liu, G., Guo, S., Hou, B., Jiang, X., Han, B., Chang, Y., and Nie, G. (2017) Identification of novel mutations in HFE, HFE2, THR2, and SLC40A1 genes in Chinese patients affected by hereditary hemochromatosis. *Int. J. Hematol.* **105**, 521–525
38. Callebaut, I., Joubrel, R., Pissard, S., Kannengiesser, C., Gérolami, V., Ged, C., Cadet, E., Cartault, F., Ka, C., Gourlaouen, I., Gourhant, L., Oudin, C., Goossens, M., Grandchamp, B., De Verneuil, H., Rochette, J., Férec, C., and Le Gac, G. (2014) Comprehensive functional annotation of 18 missense mutations found in suspected hemochromatosis type 4 patients. *Hum. Mol. Genet.* **23**, 4479–4490
39. Griffiths, W. J. H., Mayr, R., McFarlane, I., Hermann, M., Halsall, D. J., Zoller, H., and Cox, T. M. (2010) Clinical presentation and molecular pathophysiology of autosomal dominant hereditary hemochromatosis caused by a novel ferroportin mutation. *Hepatology* **51**, 788–795
40. Wallace, D. F., McDonald, C. J., Ostini, L., Iser, D., Tuckfield, A., and Subramaniam, V. N. (2017) The dynamics of hepcidin-ferroportin internalization and consequences of a novel ferroportin disease mutation. *Am. J. Hematol.* **92**, 1052–1061
41. Bach, V., Remacha, A., Altés, A., Barceló, M. J., Molina, M. A., and Baiget, M. (2006) Autosomal dominant hereditary hemochromatosis associated with two novel Ferroportin 1 mutations in Spain. *Blood Cells Mol. Dis.* **36**, 41–45
42. Cunat, S., Giansily-Blaizot, M., Bismuth, M., Blanc, F., Dereure, O., Larrey, D., Quellec, A. L., Pouderoux, P., Rose, C., Raingeard, I., Renard, E., Schved, J. F., and Aguilar-Martinez, P.; CHU Montpellier A01 2004 Working Group. (2007) Global sequencing approach for characterizing the molecular background of hereditary iron disorders. *Clin. Chem.* **53**, 2060–2069
43. Saja, K., Bignell, P., Robson, K., and Provan, D. (2010) A novel missense mutation c.470 A>C (p.D157A) in the SLC40A1 gene as a cause of ferroportin disease in a family with hyperferritinaemia. *Br. J. Haematol.* **149**, 914–916

44. Muehlenberg, K., Faltermeier, N., Lohse, P., Tannapfel, A., and Pech, O. (2014) [Family with marked hyperferritinemia as a result of hemochromatosis type 4 (ferroportin disease)]. *Z. Gastroenterol.* **52**, 1075–1080
45. Hattori, A., Miyajima, H., Tomosugi, N., Tatsumi, Y., Hayashi, H., and Wakusawa, S. (2012) Clinicopathological study of Japanese patients with genetic iron overload syndromes. *Pathol. Int.* **62**, 612–618
46. Yamashita, T., Morotomi, N., Sohda, T., Hayashi, H., Yoshida, N., Ochi, K., Ohkura, I., Karita, M., Fujiwara, H., Yamashita, H., Hattori, A., and Tatsumi, Y. (2014) A male patient with ferroportin disease B and a female patient with iron overload similar to ferroportin disease B. *Clin. J. Gastroenterol.* **7**, 260–264
47. Hetet, G., Devaux, I., Soufir, N., Grandchamp, B., and Beaumont, C. (2003) Molecular analyses of patients with hyperferritinemia and normal serum iron values reveal both L ferritin IRE and 3 new ferroportin (slc11a3) mutations. *Blood* **102**, 1904–1910
48. Kaneko, Y., Miyajima, H., Piperno, A., Tomosugi, N., Hayashi, H., Morotomi, N., Tsuchida, K., Ikeda, T., Ishikawa, A., Ota, Y., Wakusawa, S., Yoshioka, K., Kono, S., Pelucchi, S., Hattori, A., Tatsumi, Y., Okada, T., and Yamagishi, M. (2010) Measurement of serum hepcidin-25 levels as a potential test for diagnosing hemochromatosis and related disorders. *J. Gastroenterol.* **45**, 1163–1171
49. Pelucchi, S., Mariani, R., Salvioni, A., Bonfadini, S., Riva, A., Bertola, F., Trombini, P., and Piperno, A. (2008) Novel mutations of the ferroportin gene (SLC40A1): analysis of 56 consecutive patients with unexplained iron overload. *Clin. Genet.* **73**, 171–178
50. Corradini, E., Montosi, G., Ferrara, F., Caleffi, A., Pignatti, E., Barelli, S., Garuti, C., and Pietrangelo, A. (2005) Lack of enterocyte iron accumulation in the ferroportin disease. *Blood Cells Mol. Dis.* **35**, 315–318
51. Speletas, M., Kioumi, A., Loules, G., Hytioglou, P., Tsitouridis, J., Christakis, J., and Germentis, A. E. (2008) Analysis of SLC40A1 gene at the mRNA level reveals rapidly the causative mutations in patients with hereditary hemochromatosis type IV. *Blood Cells Mol. Dis.* **40**, 353–359
52. Koyama, C., Wakusawa, S., Hayashi, H., Ueno, T., Suzuki, R., Yano, M., Saito, H., and Okazaki, T. (2005) A Japanese family with ferroportin disease caused by a novel mutation of SLC40A1 gene: hyperferritinemia associated with a relatively low transferrin saturation of iron. *Intern. Med.* **44**, 990–993
53. Jouanolle, A.-M., Douabin-Gicquel, V., Halimi, C., Loréal, O., Fergelot, P., Delacour, T., de Lajarte-Thirouard, A. S., Turlin, B., Le Gall, J. Y., Cadet, E., Rochette, J., David, V., and Brissot, P. (2003) Novel mutation in ferroportin 1 gene is associated with autosomal dominant iron overload. *J. Hepatol.* **39**, 286–289
54. Pettersen, E. F., Goddard, T. D., Huang, C. C., Couch, G. S., Greenblatt, D. M., Meng, E. C., and Ferrin, T. E. (2004) UCSF Chimera—a visualization system for exploratory research and analysis. *J. Comput. Chem.* **25**, 1605–1612

Received for publication July 23, 2019.

Accepted for publication September 23, 2019.